















# Early Science from GOTHAM: Project Overview, Methods, and the Detection of Interstellar Propargyl Cyanide (HCCCH<sub>2</sub>CN) in TMC-1

Brett A. McGuire<sup>1,2,3</sup> , Andrew M. Burkhardt<sup>3</sup> , Ryan A. Loomis<sup>2</sup> , Christopher N. Shingledecker<sup>4,5</sup> , Kin Long Kelvin Lee<sup>3</sup> , Steven B. Charnley<sup>6</sup>, Martin A. Cordiner<sup>6,7</sup> , Eric Herbst<sup>8,9</sup> , Sergei Kalenskii<sup>10</sup>, Emmanuel Momjian<sup>11</sup> , Eric R. Willis<sup>8</sup> , Ci Xue<sup>8</sup> , Anthony J. Remijan<sup>2</sup> , and Michael C. McCarthy<sup>3</sup> 

<sup>1</sup> Department of Chemistry, Massachusetts Institute of Technology, Cambridge, MA 02139, USA; [brettmc@mit.edu](mailto:brettmc@mit.edu)

<sup>2</sup> National Radio Astronomy Observatory, Charlottesville, VA 22903, USA

<sup>3</sup> Center for Astrophysics | Harvard & Smithsonian, Cambridge, MA 02138, USA

<sup>4</sup> Center for Astrochemical Studies, Max Planck Institute for Extraterrestrial Physics, Garching, Germany

<sup>5</sup> Institute for Theoretical Chemistry, University of Stuttgart, Stuttgart, Germany

<sup>6</sup> Astrochemistry Laboratory and the Goddard Center for Astrobiology, NASA Goddard Space Flight Center, Greenbelt, MD 20771, USA

<sup>7</sup> Institute for Astrophysics and Computational Sciences, The Catholic University of America, Washington, DC 20064, USA

<sup>8</sup> Department of Chemistry, University of Virginia, Charlottesville, VA 22904, USA

<sup>9</sup> Department of Astronomy, University of Virginia, Charlottesville, VA 22904, USA

<sup>10</sup> Astro Space Center, Lebedev Physical Institute, Russian Academy of Sciences, Moscow, Russia

<sup>11</sup> National Radio Astronomy Observatory, Socorro, NM 87801, USA

Received 2020 March 16; revised 2020 July 13; accepted 2020 July 13; published 2020 September 1

## Abstract

We present an overview of the GBT Observations of TMC-1: Hunting Aromatic Molecules Large Program on the Green Bank Telescope. This and a related program were launched to explore the depth and breadth of aromatic chemistry in the interstellar medium at the earliest stages of star formation, following our earlier detection of benzonitrile (*c*-C<sub>6</sub>H<sub>5</sub>CN) in TMC-1. In this work, details of the observations, use of archival data, and data reduction strategies are provided. Using these observations, the interstellar detection of propargyl cyanide (HCCCH<sub>2</sub>CN) is described, as well as the accompanying laboratory spectroscopy. We discuss these results, and the survey project as a whole, in the context of investigating a previously unexplored reservoir of complex, gas-phase molecules in pre-stellar sources. A series of companion papers describe other new astronomical detections and analyses.

*Unified Astronomy Thesaurus concepts:* [Astrochemistry \(75\)](#); [Polycyclic aromatic hydrocarbons \(1280\)](#); [Chemical abundances \(224\)](#); [Interstellar medium \(847\)](#); [Dark interstellar clouds \(352\)](#); [Dense interstellar clouds \(371\)](#); [Interstellar molecules \(849\)](#)

*Supporting material:* data behind figure

## 1. Introduction, Overview, and Motivation

More than 204 individual molecular species have been detected to date in the interstellar medium (ISM; McGuire 2018). Of these, only 10 (<5%) are fully saturated—meaning they have only single bonds. It is perhaps then surprising that few aromatic molecules, which are greatly stabilized by the presence of delocalized electrons shared across their bonds, have been seen in the ISM. Indeed, despite their dominant place in terrestrial organic chemistry (Lipkus et al. 2008; Ruddigkeit et al. 2012), only two (non-fullerene) benzene-containing molecules have been detected: benzene itself (*c*-C<sub>6</sub>H<sub>6</sub>; Cernicharo et al. 2001) and, recently, benzonitrile (cyanobenzene; *c*-C<sub>6</sub>H<sub>5</sub>CN; McGuire et al. 2018).

The few detections of interstellar benzene have all been toward post-asymptotic giant branch (AGB)/pre-planetary nebula sources such as CRL 618 and SMP-LMC 11 (Cernicharo et al. 2001; Kraemer et al. 2006; Malek et al. 2012; García-Hernández et al. 2016). This finding is consistent with the broadly discussed theory of the formation of large aromatic molecules, such as the polycyclic aromatic hydrocarbons (PAHs), in the circumstellar envelopes of soot-producing, post-AGB stars: “top-down chemistry.” PAHs can then be broken down in the harsh environment until they eventually are ejected from the region with some observed distribution that includes benzene and other small benzene-containing species

(see Tielens 2008 and references therein for an extensive discussion).

Benzonitrile, however, was detected in the pre-stellar source, the Taurus Molecular Cloud 1 (TMC-1). The presence of this benzene-ring molecule in a pre-stellar source, nearly as far separated from the post-AGB phase as is possible, is therefore surprising. If the predominant source of benzene is indeed from post-AGB molecular synthesis, this would likely imply that at least a portion of the chemical inventory of this dark cloud was inherited from a previous generation of stars. Yet, it is also possible that a substantial population of benzene can be formed via a “bottom-up chemistry” from smaller organic precursors present in the cloud. Indeed, recent laboratory work has shown that plausible formation pathways to benzene and benzonitrile may exist in sources such as TMC-1 (Balucani et al. 1999; Jones et al. 2011; Lee et al. 2019; Cooke et al. 2020). Regardless of the relative dominance of these formation scenarios—and it is likely some combination of the two—the unexpected presence of large aromatic molecules in pre-stellar sources raises a number of questions.

1. Are there other aromatic species beyond benzonitrile (and, by proxy, benzene) in TMC-1?
2. What other precursors are available in TMC-1 to build these aromatic molecules in a bottom-up scenario?

3. Is this chemistry unique to TMC-1, or is it widespread throughout the early star formation process?
4. Do these species survive (and thus impact) the collapse to, and formation of, a protostar and the simultaneous chemical evolution?

To begin to address these questions, two observing programs have been undertaken with the Robert C. Byrd 100 m Green Bank Telescope (GBT) to explore more fully both the aromatic chemistry in TMC-1 specifically and at the earliest stages of the star and planet formation processes more generally.

The first program, GBT Observations of TMC-1: Hunting for Aromatic Molecules (GOTHAM), is a large-scale high-spectral resolution, high-sensitivity, large-bandwidth spectral line survey of TMC-1. The primary goals of GOTHAM are to address the first two questions by establishing the chemical inventory in this source by performing a very high-sensitivity wide-band spectral line survey, and then use this information to explore, through laboratory and modeling work, bottom-up chemistry in TMC-1. The second project, A Rigorous *K*-band Hunt for Aromatic Molecules (ARKHAM), is a high-sensitivity search for benzonitrile in pre-stellar and proto-stellar sources outside of TMC-1, addressing the second two questions.

A series of six papers provides early science results from the ongoing GOTHAM and ARKHAM programs. This paper describes the motivation behind GOTHAM, the observing strategy, calibration, and reduction of the survey data, along with the interstellar detection of propargyl cyanide ( $\text{HCCCH}_2\text{CN}$ ). Burkhardt et al. (2020) presents the first results of ARKHAM: detection of benzonitrile in four additional sources, a finding which demonstrates the widespread existence of aromatic chemistry throughout the earliest stages of star formation. Loomis et al. (2020) provides a detailed description of the fitting and velocity stacking techniques used to analyze the data, and applies these techniques to the detection of  $\text{HC}_{11}\text{N}$  in TMC-1, a long-chain polyene the detectability of which has been the subject of recent debate in the literature (Bell et al. 1997; Loomis et al. 2016; Cordiner et al. 2017). McGuire et al. (2020) presents the detections of both 1- and 2-cyanonaphthalene ( $\text{C}_{10}\text{H}_7\text{CN}$ ), the first individual PAHs detected in the ISM, in TMC-1. McCarthy et al. (2020) describes detection of 1-cyano-cyclopentadiene ( $c\text{-C}_5\text{H}_5\text{CN}$ ), a highly polar five-membered ring, in the same source. Finally, Xue et al. (2020) describes the astronomical discovery of  $\text{HC}_4\text{NC}$ , the isocyanide isomer of the commonly observed cyanopolyene  $\text{HC}_5\text{N}$ , and explores the implications for the formation pathways of these widespread molecules in the ISM.

## 2. TMC-1 Properties

The TMC is a nearby (140 pc; Onishi et al. 2002), well-studied molecular cloud complex in which 34 molecules have been detected for the first time in the ISM (McGuire 2018).<sup>12</sup> The cyanopolyene peak within this source has been shown to be particularly rich in molecular species, and is one of the reasons TMC-1 is often used as the prototypical molecular dark cloud, especially for benchmarking astrochemical models of the early evolution of chemistry before cloud collapse (Agúndez & Wakelam 2013). The chemistry of the cyanopolyene peak in particular has been of substantial interest in recent years (Gratier et al. 2016; Fuente et al. 2019). Also, the

TMC itself has seen sustained interest, especially in the areas of chemical evolution (Scibelli & Shirley 2020). Observations at a variety of wavelengths and multiple tracers suggest the effective size of the molecular emitting region is  $\sim 20''\text{--}40''$  (see, e.g., Fehér et al. 2016 and references therein).

Because it is so quiescent, TMC-1 is characterized by extremely low rotational excitation temperatures ( $T_{\text{ex}} = 5\text{--}10\text{ K}$ ) and very narrow linewidths. Kaifu et al. (2004) reported widths of  $\sim 0.4\text{ km s}^{-1}$  FWHM at a resolution that ranged from 0.22 to  $1.26\text{ km s}^{-1}$ . Observations at higher spectral resolution ( $\leq 0.05\text{ km s}^{-1}$ ) both in the GOTHAM project (Loomis et al. 2020) and in other recent work (e.g., Dobashi et al. 2018, 2019) found that lines of most species consist of multiple velocity components with widths of  $< 0.2\text{ km s}^{-1}$ . For this work, and those presented in the other GOTHAM papers, we adopt a uniform molecular hydrogen column density of  $N_7(\text{H}_2) = 10^{22}\text{ cm}^{-2}$  and a molecular hydrogen density of  $n(\text{H}_2) = 2 \times 10^4\text{ cm}^{-3}$  toward the TMC-1 cyanopolyene peak from the work of Cernicharo et al. (2018).

## 3. Observations

This paper describes the GOTHAM Large Project. Details of the ARKHAM project are provided in Burkhardt et al. (2020). The GOTHAM observations presented here were carried out between 2018 February and 2019 May on the Robert C. Byrd 100 m GBT in Green Bank, West Virginia under project codes GBT18A\_333 and GBT18B\_007. The target was TMC-1 at (J2000)  $\alpha = 04^{\text{h}}41^{\text{m}}42^{\text{s}}.50$   $\delta = +25^{\circ}41'26''.8$ . Pointing and focus observations were performed using J0530+1331 as the calibrator source at the beginning of each observing session, and every subsequent 1–2 hr, depending on the weather. Typical pointing solutions converged to  $\lesssim 5''$ . Observations were performed in ON–OFF position-switched mode with two minutes on target and two minutes off target, and an off position throw of  $1^{\circ}$ . In addition to these new observations, we have also used the data acquired for the original benzonitrile detection under project codes GBT17A-164 and GBT17A-434. The detailed observing strategy for these archival data is outlined in McGuire et al. (2018), but is largely identical to that used for the GOTHAM data. The archival data were taken in their raw form from the archive and were re-calibrated and re-reduced uniformly with the new GOTHAM observations, to ensure consistency.

### 3.1. Spectral Configuration

The full spectral coverage of the survey is shown in Figure 1. Three receivers were used to cover the frequency range of the observations, the *X*-band (8.0–11.6 GHz), *K*-band Focal Plane Array (KFPA; 18.0–27.5 GHz), and *Ka*-band (26.0–39.5 GHz) receivers. The VEGAS spectrometer was the backend for all observations (Roshi et al. 2012).

#### 3.1.1. *X*-band

In *X*-band, eight VEGAS spectrometer banks were configured in their 187.5 MHz modes with 131,072 channels corresponding to a resolution of 1.4 kHz ( $0.05\text{ km s}^{-1}$  at 9 GHz). All eight spectrometers were routed to the single beam of this dual-circular polarization receiver, and both polarizations were recorded. The half-power beamwidth (HPBW) of the GBT is  $\sim 80''$  at 9 GHz.

<sup>12</sup> This series of papers brings that total to 40, or almost 20% of all known interstellar species.

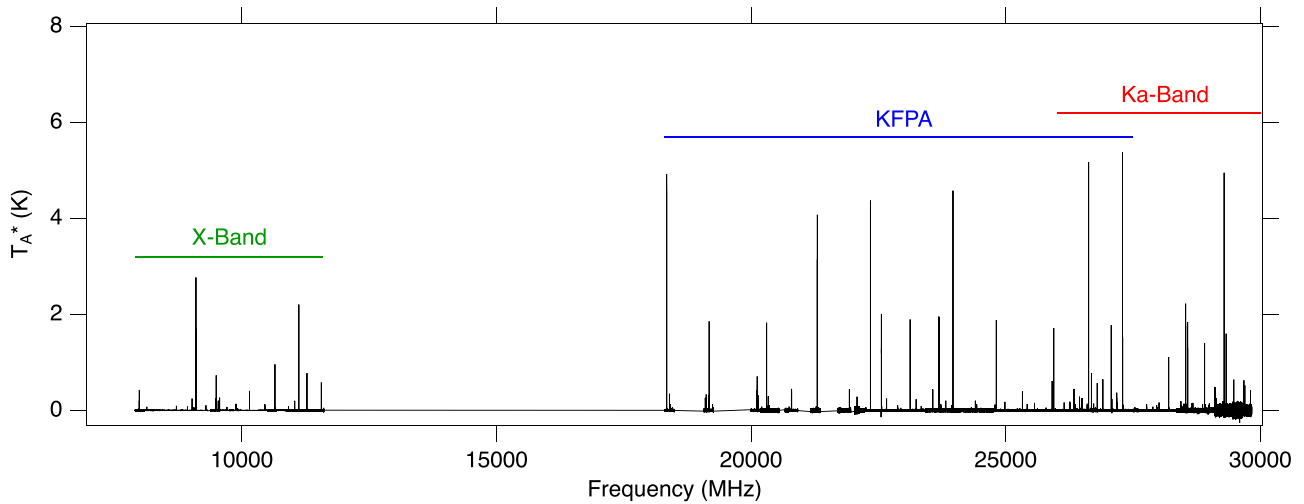


**Figure 1.** Current total coverage of the GOTHAM Large Project from the observations described here and archival observations described in McGuire et al. (2018). The receivers used in each frequency range are labeled above the spectra. The data behind the X-Band in this figure are available in machine-readable format. (The data used to create this figure are available.)

### 3.1.2. K-band

The KFPA is a seven-pixel focal plane array receiver operating from 18 to 27.5 GHz (Morgan et al. 2008). For these observations, all eight spectrometers of VEGAS were routed to the central pixel/beam of the KFPA, and both polarizations were recorded. The VEGAS spectrometer banks were configured in their 187.5 MHz modes with 131,072 channels corresponding to a resolution of 1.4 kHz ( $0.02 \text{ km s}^{-1}$  at 23 GHz). The data obtained for GOTHAM begin at 22.2 GHz; data below 22.2 GHz were obtained from the archive (GBT17A-164 and GBT17A-434). The observing strategy for these archival data is described in detail in (McGuire et al. 2018), but they have been uniformly re-reduced as part of the larger data set here. The HPBW of the GBT at 23 GHz is  $\sim 33''$ .

### 3.1.3. Ka-band

The *Ka*-band receiver is a dual-beam receiver operating from 26 to 39.5 GHz, with only a single linear polarization available per beam. Due to limitations in the IF system, only four VEGAS spectrometers can be routed to a single beam, and only the single polarization for that beam is obtained, in this case, LL. For these observations, the four VEGAS spectrometer banks were configured in their 187.5 MHz modes with 131,072 channels corresponding to a resolution of 1.4 kHz ( $0.015 \text{ km s}^{-1}$  at 28 GHz). The HPBW of the GBT at 28 GHz is  $\sim 27''$ .

## 3.2. Calibration

All three receivers are primarily calibrated by means of an internal noise diode, which we assume gives an absolute flux density calibration uncertainty of, at best,  $\sim 30\%$ . The noise diode in the X-band receiver was calibrated as recently as 2018 and referenced to Karl G. Jansky Very Large Array (VLA) flux density measurements (see <http://www.gb.nrao.edu/GBTCAL/>), and is therefore assumed to be better than 30%. We have taken several steps to improve both the absolute flux calibration of the KFPA and *Ka*-band measurements, and to ensure relative agreement between the two (and with X-band). The pointing

source, J0530+1331 was observed after every pointing and focus performed as part of the observations, using an identical spectral setup and position-switched cadence with VEGAS as would be used for the subsequent science target. Because J0530+1331 has shown long-term variability (as well as short-term variability of order  $\sim 20\%$ ; Gorshkov et al. 2016), we obtained new VLA flux density measurements of the source.

The VLA observations of J0530+1331 were carried out on 2019 May 6 at *K*-band (18–26.5 GHz) for a total of 25 minutes. The 8-bit samplers utilized in these observations delivered a total frequency coverage that spanned the range 24–26 GHz. The absolute flux density scale was set by observing the calibrator J0521+1638 (3C 138) and using the Perley–Butler 2017 flux density scale standard (Perley & Butler 2017). The elevation of both J0530+1331 and 3C 138 was near  $65^\circ$  during these observations. The calibrator source 3C 138 is also known to exhibit variability, and through regular monitoring observations with the VLA between 2016 and 2019, it was found that the flux density of 3C 138 has increased by 8% compared to the values of the Perley–Butler 2017 standard (R. Perley 2020, private communication). Accounting for this variability in 3C 138, we measured the flux density value of  $1.19 \pm 0.03 \text{ Jy}$  at 25 GHz for J0530+1331 in 2019 May. This value was then used to calibrate the GBT flux scaling.

The KFPA noise diode internal calibration is more recent than that of the *Ka*-receiver, and so we first calibrated the KFPA measurements to flux densities measured with the VLA. Because there is spectral overlap between the KFPA and *Ka*-receiver, we then use spectral line observations of the  $J = 3-2$  transition of  $\text{HCC}^{13}\text{CN}$  at 27181 MHz with both receivers to bring the *Ka*-receiver measurements into the same calibration as the KFPA. Because of the short-term variability in J0530+1331, and the differences between receivers, we still assume the calibration accuracy is only  $\sim 20\%$ , and fold this uncertainty into all calculations. This is usually the dominant source of uncertainty in our measurements. Nevertheless, we are confident that the relative calibration between receivers is much better than this number.



#### 4. Data Reduction

Initial data processing and calibration was performed using GBTIDL. Each ON–OFF position switched scan pair was corrected for Doppler tracking, calibrated to the internal noise diodes, and then placed on the atmosphere-corrected  $T_A^*$  intensity scale (Ulich & Haas 1976). When available (for X-band and the KFPA), both recorded polarizations were averaged together to improve the signal-to-noise ratio (S/N). The spectra were then manually cleaned of radio-frequency interference and artifacts. Baselines were removed with a polynomial fit of order appropriate to the baseline ripple observed, and that typically ranged from 1 to 20. In all cases, the continuum model was inspected to ensure that the line profiles, which are exceedingly narrow compared to the model, were not affected. Finally, a noise-weighted average was performed to arrive at the final spectrum.

When convolved to a uniform velocity resolution of  $0.05 \text{ km s}^{-1}$  across the spectrum (corresponding to the lowest-resolution data at X-band), the rms noise level varies from  $\sim 2$  to 20 mK, dependent entirely upon the integration time achieved at that frequency as of 2019 May 10. A uniform sensitivity of  $\sim 2 \text{ mK}$  (at  $0.05 \text{ km s}^{-1}$ ) is expected across the entire band at the completion of the project, although we make use of the full 1.4 kHz resolution when possible. A fully reduced and calibrated data set will be provided to the community upon completion of the entire survey. As there are no further data intended to be collected at X-band, that portion of the survey is considered complete and has been provided in its reduced form as the data behind Figure 1.

#### 5. Detection of Propargyl Cyanide

The laboratory rotational spectrum of propargyl cyanide<sup>13</sup> was first reported by Jones & Sheridan (1982) up to 39 GHz. Later work by Demaison et al. (1985), McNaughton et al. (1988), and Jager et al. (1990) extended the measurements to 300 GHz and included a determination of the  $^{14}\text{N}$  nuclear hyperfine parameters. The dipole moment components ( $\mu_a = 2.87 \text{ D}$ ,  $\mu_b = 2.19 \text{ D}$ ,  $\mu = 3.61 \text{ D}$ ) were derived in McNaughton et al. (1988). Based on these spectra, Lovas et al. (2006) performed an astronomical search for propargyl cyanide in TMC-1 while investigating its structural isomers cyanoallene ( $\text{CH}_2\text{CCHCN}$ ) and methylcyanoacetylene ( $\text{CH}_3\text{CCCN}$ ). Using the GBT, they set a  $1\sigma$ , beam-averaged upper limit of  $N_T = 2.8 \times 10^{11} \text{ cm}^{-2}$  for the column density of propargyl cyanide assuming  $T_{\text{ex}} = 4 \text{ K}$ , a 5 mK rms noise level for the  $4_{1,4} - 3_{1,3}$  transition at 21249 MHz, and a resolution of 6.1 kHz, equivalent to  $0.09 \text{ km s}^{-1}$ . Because the present observations cover a substantially wider frequency range at much higher sensitivity and resolution, it was necessary to systematically re-measure hyperfine-split transitions of propargyl cyanide in the laboratory up to 40 GHz so as to better match the new, high-quality astronomical data.

##### 5.1. Laboratory Measurements

To derive rest frequencies to the accuracy required for TMC-1, more than 110 hyperfine-split  $a$ - and  $b$ -type features of propargyl cyanide were measured to 2 kHz between 5 and 40 GHz (Table A1). These measurements were made with a

Fourier transform microwave spectrometer in combination with a supersonic jet discharge source, the same technique recently used to extend the high-resolution rotational spectroscopy of benzonitrile at centimeter wavelengths (McGuire et al. 2018). Strong lines of propargyl cyanide were observed using a mixture of acetylene (0.4%) and  $\text{CH}_3\text{CN}$  (0.1%) heavily diluted in Ne, and applying a voltage of 1300 V as the gas passed through the throat of the nozzle source. Relative to previous high-resolution work, lines originating from higher  $J$ , and therefore higher frequency, were observed in the present study. By varying 10 parameters in a standard A-reduced asymmetric top Hamiltonian (Watson 1977) with hyperfine interactions—the three rotational constants, the five quartic centrifugal distortion constants, and two tensor terms that describe the nitrogen hyperfine structure—it was possible to achieve a fit rms (2.5 kHz) that was comparable to the measurement uncertainty. From these best-fit constants (Table A2), the astronomically most intense hyperfine-split transitions of this species could now be calculated to  $0.03 \text{ km s}^{-1}$  or better, equivalent to about 1/5 of the linewidth in TMC-1, or the width of a single channel in the astronomical survey.

##### 5.2. Observational Analysis

Full details of the observational analysis method are provided in Loomis et al. (2020). In short, we first perform a Markov chain Monte Carlo (MCMC) fit to the strongly detected  $\text{HC}_9\text{N}$  cyanopolyne and to  $c\text{-C}_6\text{H}_5\text{CN}$ . We detect four distinct velocity components contributing to the overall signal for lines of these species, and derive velocities ( $v_{\text{lsr}}$ ), column densities ( $N_T$ ), and source sizes ( $\theta_s$ ) simultaneously with an excitation temperature ( $T_{\text{ex}}$ ) and linewidth ( $\Delta V$ ) following the conventions of Turner (1991) which include corrections for optical depth. The values of  $v_{\text{lsr}}$ ,  $\theta_s$ ,  $T_{\text{ex}}$ , and  $\Delta V$  are then used as priors for MCMC analyses of other species with fewer and/or weaker lines, with  $T_{\text{ex}}$  and  $\Delta V$  assumed to be the same for all velocity components.  $\text{HC}_9\text{N}$  is used as a starting point for linear molecules while  $c\text{-C}_6\text{H}_5\text{CN}$  is used for cyclic species.

Using the priors from  $\text{HC}_9\text{N}$ , four lines belonging to propargyl cyanide were detected and fit above the present noise level of the observations: the  $4_{1,3} - 3_{1,2}$ ,  $5_{1,5} - 4_{1,4}$ ,  $5_{0,5} - 4_{0,4}$ , and  $5_{1,4} - 4_{1,3}$  hyperfine-split transitions. These are shown in Figure 2. More than 3700 transitions of propargyl cyanide fall within the range of GOTHAM’s coverage, however, and contribute to the total flux seen for this molecule. The MCMC analysis included all of these transitions (see Appendix B), and resulted in a significant detection of propargyl cyanide emission in three of the four velocity components in which  $\text{HC}_9\text{N}$  is found. The resulting physical parameters, column densities, and excitation temperatures are given in Table 1.

Using these parameters, we then perform an intensity and noise-weighted average (“stack”) of both the observations and the best-fit model spectra in velocity-space, resulting in a substantial increase in S/N on a channel-by-channel basis. This spectrum encapsulates the total flux of emission from propargyl cyanide contained within the bandwidth of GOTHAM, rather than only the flux coming from lines seen above the local noise level of the observations. This is shown in Figure 3 (left). Finally, to determine the overall significance of the detection, we use the stacked model as a matched filter which is pushed through the stacked observations. The resulting impulse

<sup>13</sup> Propargyl cyanide has several alternative names in the chemical literature including 3-butyne nitrile and 1-cyanoprop-2-yne.

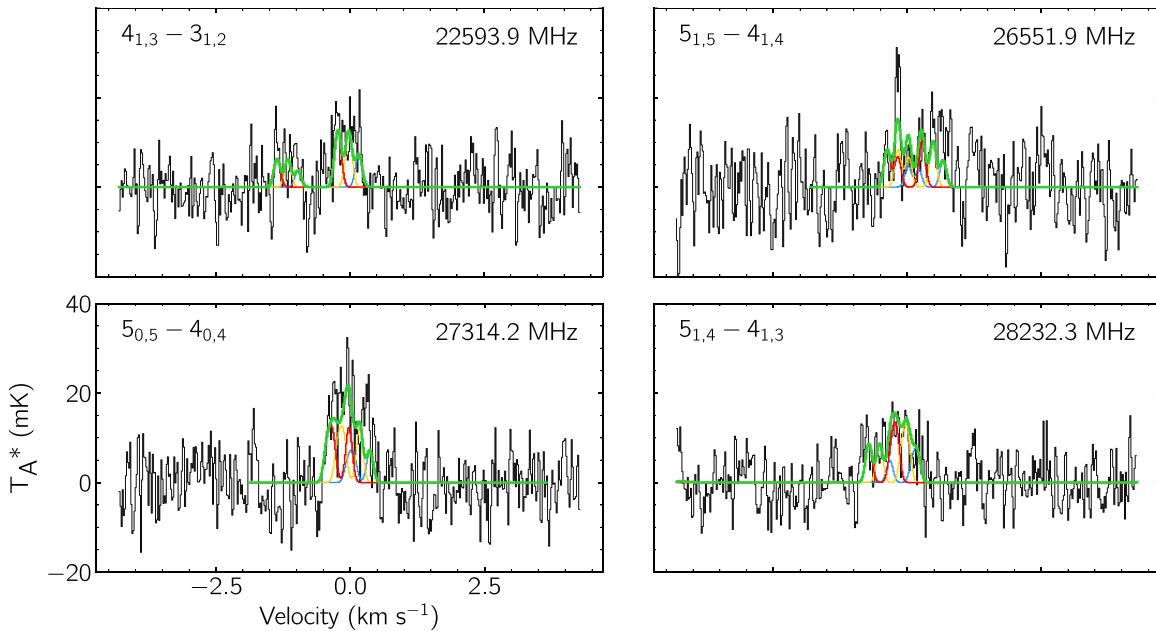


**Figure 2.** Individual line detections of propargyl cyanide in the GOTHAM data. The spectra (black) are displayed in velocity space relative to  $5.8 \text{ km s}^{-1}$ , and using the rest frequency given in the top right of each panel. Quantum numbers are given in the top left of each panel, neglecting hyperfine splitting. The best-fit model to the data, including all velocity components, is overlaid in green. Simulated spectra of the individual velocity components are shown in: blue ( $5.615 \text{ km s}^{-1}$ ), gold ( $5.804 \text{ km s}^{-1}$ ), red ( $6.005 \text{ km s}^{-1}$ ). See Table 1.

response function represents the minimum statistical significance of the detection and is shown in Figure 3 (right).

### 5.3. Astrochemical Modeling

In order to better understand the chemistry of propargyl cyanide in cold cores, we have simulated TMC-1 using astrochemical codes. Specifically, for this study we have used the NAUTILUS-v1.1 program (Ruaud et al. 2016) along with a modified version of the KIDA 2014 network (Wakelam et al. 2015) also used in the analysis of the other species detected in the GOTHAM and ARKHAM surveys (Burkhardt et al. 2020; Loomis et al. 2020; McCarthy et al. 2020; McGuire et al. 2020; Xue et al. 2020). Typical TMC-1 physical conditions were used, including  $T_{\text{gas}} = T_{\text{dust}} = 10 \text{ K}$ , a gas density of  $2 \times 10^4 \text{ cm}^{-3}$ , and a standard cosmic ray ionization rate of  $1.3 \times 10^{-17} \text{ s}^{-1}$ . Initial elemental abundances were taken from Hincelin et al. (2011) with the exception of atomic oxygen, where we utilize a slightly carbon rich  $\text{C/O} \approx 1.1$  and  $x(\text{O})_{t=0} \approx 1.5 \times 10^{-4}$ , as described in Loomis et al. (2020).

The results of our simulations are shown in Figure 4. In our network, propargyl cyanide is formed mainly via the reaction



This reaction has, to the best of our knowledge, not been studied in detail. However, based on work by Smith et al. (2006), we assume it occurs barrierlessly since the difference between the ionization energy of propyne,  $10.36 \text{ eV}$  (Lias et al. 2020), and the electron affinity of the cyano radical,  $3.86 \text{ eV}$  (Bradforth et al. 1993), is less than  $\sim 9 \text{ eV}$ . Based on our assumption that reaction (1) is a barrierless process, we have included it in our network with the single-collision rate coefficient of  $3 \times 10^{-10} \text{ cm}^3 \text{ s}^{-1}$ .

By a similar line of reasoning, we do not include the analogous reactions involving the propargyl radical,  $\text{CH}_2\text{CCH}$ ,

namely,



since the difference between the ionization energies of the closed-shell reactants and the propargyl radical is greater than  $9 \text{ eV}$  in both cases. Given the likely presence of activation energies for reactions (2) and (3), we did not attempt to quantitatively estimate their effect on the abundance propargyl cyanide, though our assumption here is that the rate coefficients will be much smaller than that of reaction (1).

An additional grain-surface formation route involving the 1-cyano propargyl radical,  $\text{HCCCHCN}$ , i.e.,



was also included. Here, the 1-cyano propargyl radical precursor is formed in the gas and on grains via the reaction of carbon atoms with vinyl cyanide (Guo et al. 2006), with the barrierless gas-phase formation route also being assumed to occur at the collision rate of  $3 \times 10^{-10} \text{ cm}^3 \text{ s}^{-1}$  in our network. For reaction (4), and indeed for all such diffusive surface reactions, rate coefficients were calculated using the formula described in Section 2.3 of Ruaud et al. (2016); however, given the low dust temperatures in our simulations and the small fraction of grain-surface  $\text{HCCCH}_2\text{CN}$  that is non-thermally desorbed, the overall contribution of (4) to the gas-phase abundance of propargyl cyanide was negligible compared with (1). Once formed, gas-phase propargyl cyanide is destroyed via reaction with ions, with rate coefficients calculated using the formula given in Woon & Herbst (2009).

As one can see in Figure 4, our calculated abundances of propargyl cyanide qualitatively match the observationally derived values to within a factor of a few. In general, we find that the abundances of species such as propargyl cyanide as

**Table 1**  
Propargyl Cyanide Best-fit Parameters from MCMC Analysis

Component	$v_{\text{lsr}}$ (km s <sup>-1</sup> )	Size ( $''$ )	$N_T^a$ ( $10^{11}$ cm <sup>-2</sup> )	$T_{\text{ex}}$ (K)	$\Delta V$ (km s <sup>-1</sup> )
C1	$5.615^{+0.016}_{-0.016}$	$207^{+133}_{-122}$	$2.07^{+0.39}_{-0.31}$		
C2	$5.804^{+0.009}_{-0.010}$	$130^{+178}_{-84}$	$3.59^{+1.14}_{-0.44}$	$6.5^{+0.3}_{-0.3}$	$0.144^{+0.012}_{-0.010}$
C3	$6.005^{+0.008}_{-0.008}$	$192^{+131}_{-116}$	$3.56^{+0.53}_{-0.36}$		
$N_T$ (Total) <sup>b</sup>			$9.21^{+1.31}_{-0.65} \times 10^{11}$ cm <sup>-2</sup>		

**Notes.** The quoted uncertainties represent the 16th and 84th percentile ( $1\sigma$  for a Gaussian distribution) uncertainties.

<sup>a</sup> Column density values are highly covariant with the derived source sizes. The marginalized uncertainties on the column densities are therefore dominated by the largely unconstrained nature of the source sizes, and not by the signal-to-noise of the observations. See Figure A1 for a covariance plot, and Loomis et al. (2020) for a detailed explanation of the methods used to constrain these quantities and derive the uncertainties.

<sup>b</sup> Uncertainties derived by adding the uncertainties of the individual components in quadrature.

well as other unsaturated species such as the cyanopolyynes—with the exception of HC<sub>11</sub>N (Loomis et al. 2020)—are much better reproduced than the more complex, aromatic 1-/2-cyanonaphthalene (McGuire et al. 2020), benzonitrile (Burkhardt et al. 2020), and 1-cyano-cyclopentadiene (McCarthy et al. 2020), all of which are severely underproduced. This striking difference in how well our models reproduce the abundances of these species suggests a fundamental shortcoming in how the chemistry of cyclic molecules, generally, is included in our network and, in particular, that there are additional top-down or bottom-up mechanisms that could efficiently form the aromatic precursors.

Furthermore, it is possible that the formation of these aromatic species relies on the cyclization of long carbon chain species. Detections of both cyclic species and their potential cyclization precursors are therefore important for providing observational constraints on the efficacy of this process. As such, the likely imminent detection of more partially saturated carbon chains, such as propargyl cyanide, as the GOTHAM survey progresses will provide a fantastic resource of intermediate species for chemical models to compare to when considering a bottom-up (cyclization) formation route for cyclic molecules.

## 6. Discussion

The data set used in these six first-results papers represents only ~30% of the eventual data that will be collected for the GOTHAM project. Despite this, and despite covering less total bandwidth, GOTHAM has produced detections of a number of new interstellar molecules that were not seen in the previous work by Kaifu et al. (2004). This is true even when applying stacking techniques. For example, only a small hint of the presence of *c*-C<sub>6</sub>H<sub>5</sub>CN was seen in stacked data from Kaifu et al. (2004) in the detection presented by McGuire et al. (2018), despite the former work covering more than an order of magnitude more bandwidth.

The parameters derived for *c*-C<sub>6</sub>H<sub>5</sub>CN in this analysis are substantially improved over the prior measurements reported in McGuire et al. (2018) due to the increased sensitivity and number of observed transitions (see Appendix A). These new parameters shed some light on why our survey is detecting so many new molecules beyond what is accessible from the Kaifu et al. (2004) survey. We find that the velocity component which accounts for nearly half of the observed column of *c*-C<sub>6</sub>H<sub>5</sub>CN has a source size of  $65^{+20}_{-13}''$ . For comparison, at 25 GHz the GBT HPBW is ~30'', whereas the Nobeyama 45 m HPBW

used for the Kaifu et al. (2004) work is ~67''. This would result in a factor of ~2 difference in the line intensity of this component due to beam dilution, and is likely the main reason why *c*-C<sub>6</sub>H<sub>5</sub>CN was not observed in the Kaifu et al. (2004) survey.

Based on this simple geometric argument, and the range of source sizes we are finding, the observed intensities of rotational lines of other nitrile molecules are expected to be 2–5 times higher with the GBT than if they had been observed with the Nobeyama telescope. Detection of lines from rare isotopic (<sup>13</sup>C and <sup>15</sup>N) species of HC<sub>5</sub>N and HC<sub>7</sub>N in the same observation where *c*-C<sub>6</sub>H<sub>5</sub>CN was found provides additional evidence for the advantage of a larger telescope (Burkhardt et al. 2018). A further increase in sensitivity was achieved by observing at spectral resolution that is appropriate in this narrow line source. The resolution in the Nobeyama survey of 0.22–1.26 km s<sup>-1</sup> was frequently a factor of 2–4 times too low for the very sharp spectral lines in TMC-1 (0.1–0.3 km s<sup>-1</sup> FWHM). When combined with the sensitivity of the GOTHAM observations, we expect that, in general, our detection limits should be roughly an order of magnitude better than those of Kaifu et al. (2004).

Because the observations span a factor of ~3 in frequency (8–29 GHz), they also span a factor of ~3 in GBT beam size. As a result, for species with transitions observed across that range of frequencies and beam sizes, such as benzonitrile and the cyanopolyynes discussed above, the effects of beam dilution can be modeled and the effective source sizes used as parameters in the fits. Still, the source sizes are often the dominant sources of error in our MCMC fits (Loomis et al. 2020). This is seen quite strongly in the detection of propargyl cyanide presented here. Because most of the flux from this molecule is concentrated in our *K*-band observations, the source sizes are relatively unconstrained (Table 1 and Figure A1). Observing the source structure directly would substantially improve the certainty in our measurements of column densities and excitation temperatures.

Unfortunately, preliminary efforts to do so have proven difficult. The emission is too extended to achieve meaningful constraints with GBT maps at frequency <50 GHz. Early indications are that proof-of-concept observations with the VLA in its most compact D-configuration are proving difficult to calibrate and will lack the surface brightness sensitivity to robustly constrain these source sizes even for bright cyanopolyne features. In the short term, the most profitable avenue is likely to be maps of cyanopolyynes in *W*-band (>85 GHz) with the GBT, providing resolutions of ~10''. Longer term, the

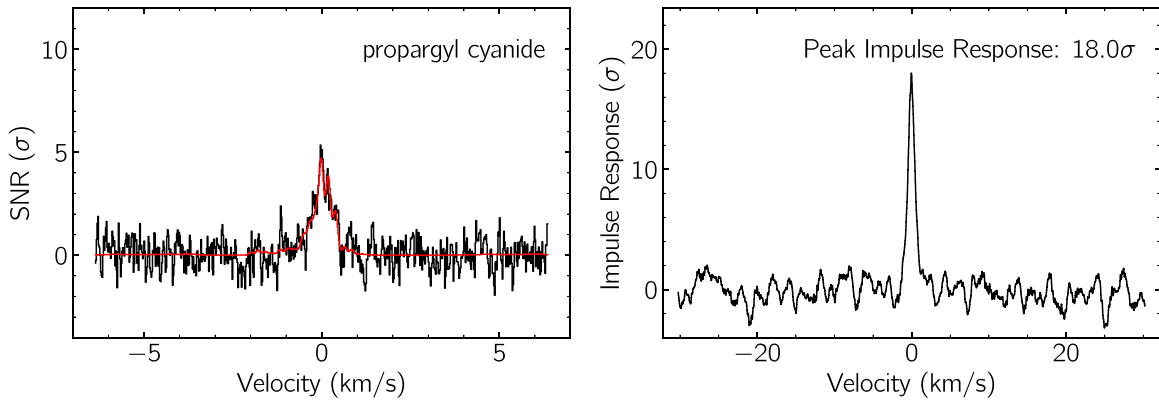


**Figure 3.** Left: velocity-stacked spectra of propargyl cyanide in black, with the corresponding stack of the simulation using the best-fit parameters to the individual lines in red. The data have been uniformly sampled to a resolution of  $0.02 \text{ km s}^{-1}$ . The intensity scale is the signal-to-noise ratio of the spectrum at any given velocity. Right: impulse response function of the stacked spectrum using the simulated line profile as a matched filter. The intensity scale is the signal-to-noise ratio of the response function when centered at a given velocity. The peak of the impulse response function provides a minimum significance for the detection of  $18.0\sigma$ . See Loomis et al. (2020) for details.

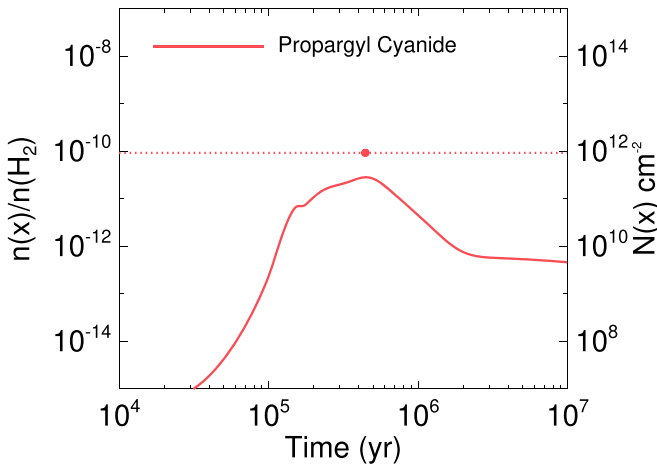


**Figure 4.** Calculated abundance of propargyl cyanide (solid line) in our TMC-1 simulation. Abundances from the MCMC analysis are represented by the dotted line and time of peak abundance by the filled circle. Note: observational errors given in Table 1 are not visible at the scale used.

central core of the next-generation VLA may provide the needed sensitivity and resolution at lower frequencies (Selina et al. 2018).

## 7. Conclusions

Motivated by the detection of *c*-C<sub>6</sub>H<sub>5</sub>CN in TMC-1, we have begun a large-scale effort to conduct a high-resolution, high-sensitivity spectral line survey of the source using the GBT. We have presented here an overview of the survey and details of the data reduction procedure. The data set shown here represents only  $\sim 30\%$  of the total survey. The detection of propargyl cyanide (HCCCH<sub>2</sub>CN) for the first time in the ISM is presented here. Based on our astrochemical modeling, the presence of propargyl cyanide suggests several additional unsaturated  $-\text{CN}$ -containing hydrocarbons may be good targets for interstellar detection. Using a combination of MCMC fitting techniques and matched filtering algorithms, an additional five new species are also seen from this survey. We expect to detect several additional new molecules from the completed set of observations. The dominant source of uncertainty is the underlying source size structure.

The authors thank the anonymous referees for their comments, which have improved the quality of this work. The authors thank D. Frayer, J. Skipper, A. Bonsall, and the staff of the Green Bank Observatory for support with observations, data reduction, and calibration strategies. A.M.B. acknowledges support from the Smithsonian Institution as a Submillimeter Array (SMA) Fellow. M.C.M. and K.L.K. Lee acknowledge support from NSF grant AST-1615847 and NASA grant 80NSSC18K0396. Support for B.A.M. was provided by NASA through Hubble Fellowship grant #HST-HF2-51396 awarded by the Space Telescope Science Institute, which is operated by the Association of Universities for Research in Astronomy, Inc., for NASA, under contract NAS5-26555. C.N.S. thanks the Alexander von Humboldt Stiftung/Foundation for their generous support, as well as V. Wakelam for use of the NAUTILUS v1.1 code. C.X. is a Grote Reber Fellow, and support for this work was provided by the NSF through the Grote Reber Fellowship Program administered by Associated Universities, Inc./National Radio Astronomy Observatory and the Virginia Space Grant Consortium. E.H. thanks the National Science Foundation for support through grant AST 1906489. M.C.M. and K.L.K.L. acknowledge financial support from NSF grants AST-1908576, AST-1615847, and NASA grant 80NSSC18K0396. S.B.C. and M.A.C. were supported by the NASA Astrobiology Institute through the Goddard Center for Astrobiology. The National Radio Astronomy Observatory is a facility of the National Science Foundation operated under cooperative agreement by Associated Universities, Inc.

## Appendix A Laboratory Measurements

This appendix includes the newly measured laboratory frequencies of propargyl cyanide (Table A1), the best-fit spectroscopic constants (Table A2), the corner plots for propargyl cyanide (Figure A1), and the analysis results for benzonitrile (Tables A3, Figures A2–A4).



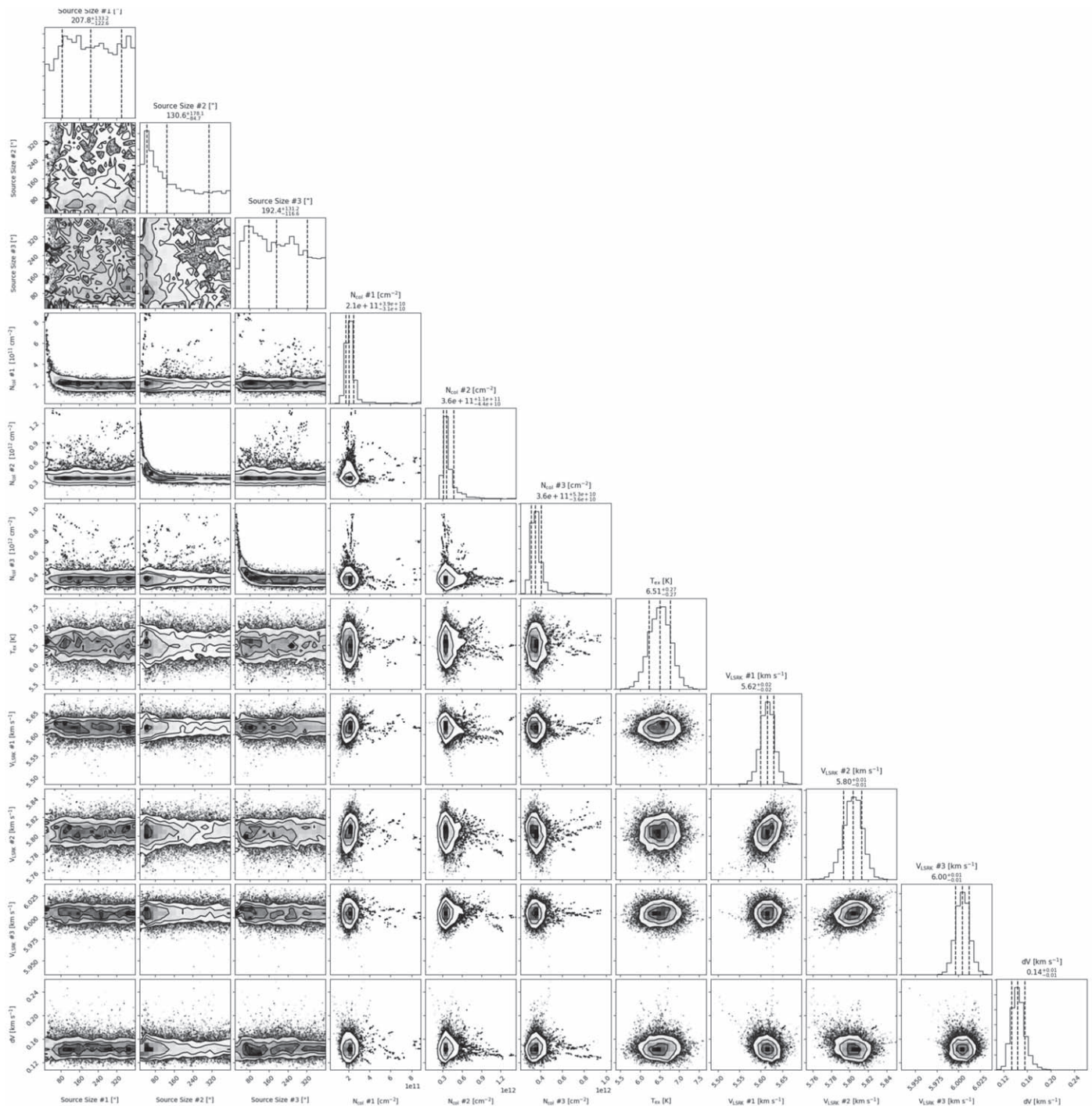


**Figure A1.** Parameter covariances and marginalized posterior distributions for the propargyl cyanide MCMC fit; 16th, 50th, and 84th confidence intervals (corresponding to  $\pm 1\sigma$  for a Gaussian posterior distribution) are shown as vertical lines.

### A.1. Propargyl Cyanide Results

#### A.2. Benzonitrile Results

The results of our MCMC fit to the data set for *c*-C<sub>6</sub>H<sub>5</sub>CN are provided below, and are substantially more robust than

those achieved in the initial detection from McGuire et al. (2018). The best-fit parameters are given in Table A3 with the associated corner plot shown in Figure A4. The individually detected lines are shown in Table A2. The stacked detection and matched-filter response are shown in Figure A3.



**Table A1**

Measured Hyperfine-split Rotational Transitions of Ground State Propargyl Cyanide

Transition		Frequency <sup>a</sup> (MHz)	Obs.-Calc <sup>b</sup> (MHz)
$J''_{Ka,Kc} \rightarrow J''_{Ka,Kc}$	$F' \rightarrow F''$		
$1_{0,1} \rightarrow 0_{0,0}$	1 → 1	5482.2420(20)	-0.0014
$1_{0,1} \rightarrow 0_{0,0}$	2 → 1	5482.9248(20)	0.0004
$1_{1,1} \rightarrow 2_{0,2}$	2 → 3	5949.1197(20)	-0.0005
$2_{1,2} \rightarrow 1_{1,1}$	2 → 1	10628.9235(20)	-0.0050
$2_{1,2} \rightarrow 1_{1,1}$	2 → 2	10628.9940(20)	0.0010
$2_{1,2} \rightarrow 1_{1,1}$	3 → 2	10629.6531(20)	-0.0003
$2_{1,2} \rightarrow 1_{1,1}$	1 → 1	10629.9537(20)	-0.0021
$2_{1,2} \rightarrow 1_{1,1}$	1 → 0	10630.1174(20)	0.0002
$2_{0,2} \rightarrow 1_{0,1}$	2 → 2	10959.9212(20)	-0.0016
$2_{0,2} \rightarrow 1_{0,1}$	1 → 0	10960.0450(20)	-0.0002
$2_{0,2} \rightarrow 1_{0,1}$	2 → 1	10960.6057(20)	0.0020
$2_{0,2} \rightarrow 1_{0,1}$	3 → 2	10960.6587(20)	0.0006
$2_{0,2} \rightarrow 1_{0,1}$	1 → 1	10961.7465(20)	-0.0011
$2_{1,1} \rightarrow 1_{1,0}$	2 → 1	11301.6338(20)	0.0017
$2_{1,1} \rightarrow 1_{1,0}$	1 → 1	11301.7364(20)	-0.0035
$2_{1,1} \rightarrow 1_{1,0}$	3 → 2	11302.3184(20)	0.0008
$2_{1,1} \rightarrow 1_{1,0}$	1 → 0	11303.2787(20)	-0.0020
$5_{0,5} \rightarrow 4_{1,4}$	4 → 3	11854.8251(20)	0.0026
$5_{0,5} \rightarrow 4_{1,4}$	6 → 5	11854.9046(20)	0.0000
$5_{0,5} \rightarrow 4_{1,4}$	5 → 4	11855.0503(20)	-0.0017
$3_{1,3} \rightarrow 2_{1,2}$	3 → 2	15940.9373(20)	0.0010
$3_{1,3} \rightarrow 2_{1,2}$	2 → 1	15941.0901(20)	-0.0013
$3_{1,3} \rightarrow 2_{1,2}$	4 → 3	15941.1534(20)	0.0016
$3_{0,3} \rightarrow 2_{0,2}$	3 → 3	16427.6447(20)	-0.0013
$3_{0,3} \rightarrow 2_{0,2}$	2 → 1	16428.2776(20)	-0.0013
$3_{0,3} \rightarrow 2_{0,2}$	3 → 2	16428.3822(20)	0.0009
$3_{0,3} \rightarrow 2_{0,2}$	4 → 3	16428.4189(20)	0.0015
$3_{0,3} \rightarrow 2_{0,2}$	2 → 2	16429.4185(20)	-0.0043
$3_{1,2} \rightarrow 2_{1,1}$	3 → 2	16949.8815(20)	-0.0016
$3_{1,2} \rightarrow 2_{1,1}$	4 → 3	16950.0758(20)	-0.0009
$3_{1,2} \rightarrow 2_{1,1}$	2 → 1	16950.1289(20)	-0.0013
$1_{1,0} \rightarrow 1_{0,1}$	1 → 0	17245.6455(20)	-0.0001
$1_{1,0} \rightarrow 1_{0,1}$	0 → 1	17245.8069(20)	-0.0003
$1_{1,0} \rightarrow 1_{0,1}$	2 → 2	17246.0536(20)	0.0029
$1_{1,0} \rightarrow 1_{0,1}$	1 → 1	17247.3477(20)	-0.0003
$2_{1,1} \rightarrow 2_{0,2}$	2 → 1	17587.2342(20)	0.0017
$2_{1,1} \rightarrow 2_{0,2}$	1 → 1	17587.3394(20)	-0.0009
$2_{1,1} \rightarrow 2_{0,2}$	3 → 3	17587.7128(20)	0.0025
$2_{1,1} \rightarrow 2_{0,2}$	2 → 2	17588.3772(20)	0.0008
$3_{1,2} \rightarrow 3_{0,3}$	2 → 2	18109.1948(20)	0.0032
$3_{1,2} \rightarrow 3_{0,3}$	4 → 4	18109.3717(20)	0.0021
$4_{1,3} \rightarrow 4_{0,4}$	3 → 3	18821.9361(20)	0.0008
$4_{1,3} \rightarrow 4_{0,4}$	5 → 5	18822.0522(20)	0.0007
$4_{1,3} \rightarrow 4_{0,4}$	4 → 4	18822.5011(20)	-0.0023
$4_{1,4} \rightarrow 3_{1,3}$	4 → 3	21248.8749(20)	0.0020
$4_{1,4} \rightarrow 3_{1,3}$	3 → 2	21248.9181(20)	0.0007
$4_{1,4} \rightarrow 3_{1,3}$	5 → 4	21248.9752(20)	0.0022
$4_{0,4} \rightarrow 3_{0,3}$	3 → 2	21881.1459(20)	0.0016
$4_{0,4} \rightarrow 3_{0,3}$	4 → 3	21881.1801(20)	0.0014
$4_{0,4} \rightarrow 3_{0,3}$	5 → 4	21881.2077(20)	-0.0006
$4_{2,3} \rightarrow 3_{2,2}$	4 → 3	21928.8705(20)	0.0001
$4_{2,3} \rightarrow 3_{2,2}$	5 → 4	21929.1814(20)	0.0001
$4_{2,3} \rightarrow 3_{2,2}$	3 → 2	21929.2619(20)	0.0006
$4_{2,2} \rightarrow 3_{2,1}$	4 → 3	21978.4755(20)	-0.0022
$4_{2,2} \rightarrow 3_{2,1}$	5 → 4	21978.7757(20)	-0.0006
$1_{1,1} \rightarrow 0_{0,0}$	0 → 1	22392.6027(20)	-0.0031
$1_{1,1} \rightarrow 0_{0,0}$	2 → 1	22392.7013(20)	-0.0014
$1_{1,1} \rightarrow 0_{0,0}$	1 → 1	22392.7656(20)	-0.0016

**Table A1**

(Continued)

Transition		Frequency <sup>a</sup> (MHz)	Obs.-Calc <sup>b</sup> (MHz)
$J''_{Ka,Kc} \rightarrow J''_{Ka,Kc}$	$F' \rightarrow F''$		
$4_{1,3} \rightarrow 3_{1,2}$	4 → 3	22593.8025(20)	-0.0015
$4_{1,3} \rightarrow 3_{1,2}$	3 → 2	22593.8892(20)	0.0012
$4_{1,3} \rightarrow 3_{1,2}$	5 → 4	22593.8892(20)	-0.0011
$7_{0,7} \rightarrow 6_{1,6}$	6 → 5	24279.3482(20)	-0.0018
$7_{0,7} \rightarrow 6_{1,6}$	8 → 7	24279.4058(20)	0.0024
$5_{1,5} \rightarrow 4_{1,4}$	5 → 4	26551.8836(20)	-0.0021
$5_{1,5} \rightarrow 4_{1,4}$	4 → 3	26551.9079(20)	0.0047
$5_{1,5} \rightarrow 4_{1,4}$	6 → 5	26551.9460(20)	0.0024
$5_{0,5} \rightarrow 4_{0,4}$	4 → 3	27314.1358(20)	-0.0042
$5_{0,5} \rightarrow 4_{0,4}$	5 → 4	27314.1545(20)	0.0049
$5_{0,5} \rightarrow 4_{0,4}$	6 → 5	27314.1773(20)	0.0001
$5_{2,4} \rightarrow 4_{2,3}$	6 → 5	27404.8830(20)	0.0060
$5_{2,4} \rightarrow 4_{2,3}$	4 → 3	27404.8924(20)	-0.0015
$5_{2,3} \rightarrow 4_{2,2}$	6 → 5	27503.8557(20)	0.0065
$2_{1,2} \rightarrow 1_{0,1}$	2 → 2	27538.7684(20)	-0.0029
$2_{1,2} \rightarrow 1_{0,1}$	3 → 2	27539.4316(20)	-0.0001
$2_{1,2} \rightarrow 1_{0,1}$	2 → 1	27539.4485(20)	-0.0038
$2_{1,2} \rightarrow 1_{0,1}$	1 → 1	27540.4816(20)	0.0020
$5_{1,4} \rightarrow 4_{1,3}$	5 → 4	28232.2441(20)	0.0015
$5_{1,4} \rightarrow 4_{1,3}$	4 → 3	28232.2760(20)	-0.0064
$5_{1,4} \rightarrow 4_{1,3}$	6 → 5	28232.2937(20)	0.0025
$8_{0,8} \rightarrow 7_{1,7}$	7 → 6	30590.8950(20)	-0.0020
$8_{0,8} \rightarrow 7_{1,7}$	9 → 8	30590.9372(20)	-0.0034
$8_{0,8} \rightarrow 7_{1,7}$	8 → 7	30591.1322(20)	0.0049
$6_{1,6} \rightarrow 5_{1,5}$	6 → 5	31848.9679(20)	-0.0024
$6_{1,6} \rightarrow 5_{1,5}$	5 → 4	31848.9850(20)	0.0057
$6_{1,6} \rightarrow 5_{1,5}$	7 → 6	31849.0099(20)	0.0011
$6_{0,6} \rightarrow 5_{0,5}$	6 → 5	32722.7003(20)	0.0004
$6_{0,6} \rightarrow 5_{0,5}$	5 → 4	32722.7003(20)	-0.0028
$6_{0,6} \rightarrow 5_{0,5}$	7 → 6	32722.7262(20)	-0.0012
$6_{2,5} \rightarrow 5_{2,4}$	6 → 5	32876.1312(20)	-0.0030
$6_{2,5} \rightarrow 5_{2,4}$	7 → 6	32876.2340(20)	0.0008
$6_{2,5} \rightarrow 5_{2,4}$	5 → 4	32876.2340(20)	0.0006
$6_{2,4} \rightarrow 5_{2,3}$	6 → 5	33048.6853(20)	-0.0019
$6_{2,4} \rightarrow 5_{2,3}$	5 → 4	33048.7660(20)	0.0001
$6_{2,4} \rightarrow 5_{2,3}$	7 → 6	33048.7660(20)	-0.0014
$6_{1,5} \rightarrow 5_{1,4}$	6 → 5	33863.7162(20)	0.0031
$6_{1,5} \rightarrow 5_{1,4}$	5 → 4	33863.7298(20)	-0.0069
$6_{1,5} \rightarrow 5_{1,4}$	7 → 6	33863.7493(20)	0.0042
$7_{1,7} \rightarrow 6_{1,6}$	7 → 6	37139.2049(20)	0.0027
$7_{1,7} \rightarrow 6_{1,6}$	6 → 5	37139.2049(20)	-0.0034
$7_{1,7} \rightarrow 6_{1,6}$	8 → 7	37139.2294(20)	-0.0012
$4_{1,4} \rightarrow 3_{0,3}$	4 → 3	37340.2769(20)	0.0005
$4_{1,4} \rightarrow 3_{0,3}$	3 → 2	37340.4631(20)	0.0012
$7_{0,7} \rightarrow 6_{0,6}$	7 → 6	38102.6913(20)	-0.0042
$7_{0,7} \rightarrow 6_{0,6}$	8 → 7	38102.7255(20)	0.0016
$7_{2,6} \rightarrow 6_{2,5}$	7 → 6	38342.3108(20)	-0.0020
$7_{2,6} \rightarrow 6_{2,5}$	6 → 5	38342.3754(20)	0.0017
$7_{2,6} \rightarrow 6_{2,5}$	8 → 7	38342.3754(20)	-0.0030
$7_{2,5} \rightarrow 6_{2,4}$	7 → 6	38616.6908(20)	-0.0008
$7_{2,5} \rightarrow 6_{2,4}$	6 → 5	38616.7262(20)	-0.0031
$7_{2,5} \rightarrow 6_{2,4}$	8 → 7	38616.7369(20)	0.0014
$7_{1,6} \rightarrow 6_{1,5}$	7 → 6	39486.5877(20)	0.0031
$7_{1,6} \rightarrow 6_{1,5}$	8 → 7	39486.6108(20)	0.0024

**Notes.**<sup>a</sup> Estimated experimental uncertainties ( $1\sigma$ ) are in units of the last significant digit.<sup>b</sup> Calculated frequencies derived from the best-fit constants listed in Table A2.

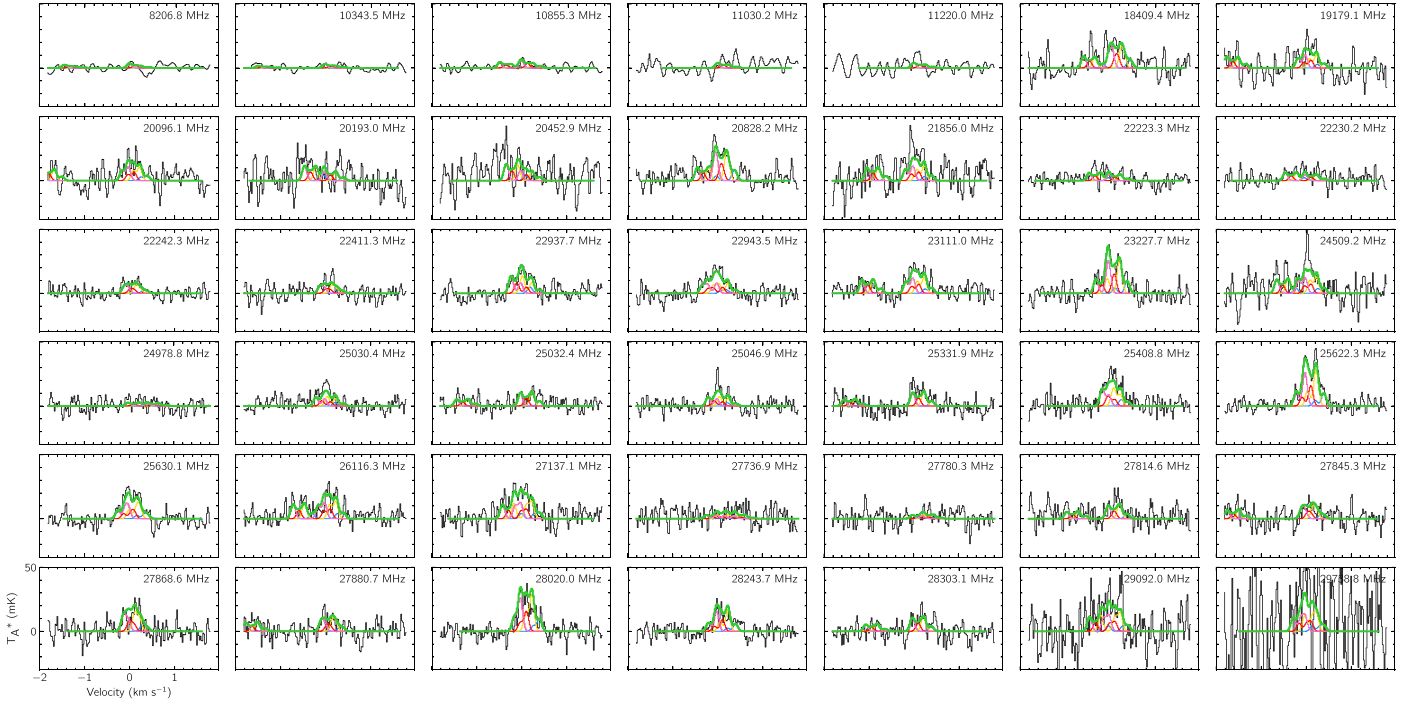


**Figure A2.** Individual line detections of  $c\text{-C}_6\text{H}_5\text{CN}$  in the GOTHAM data. The spectra (black) are displayed in velocity-space relative to  $5.8 \text{ km s}^{-1}$ , and using the rest frequency given in the top right of each panel. The best-fit model to the data, including all velocity components, is overlaid in green. Simulated spectra of the individual velocity components are shown in: blue ( $5.595 \text{ km s}^{-1}$ ), gold ( $5.764 \text{ km s}^{-1}$ ), red ( $5.886 \text{ km s}^{-1}$ ), and violet ( $6.017 \text{ km s}^{-1}$ ). See Table A3.

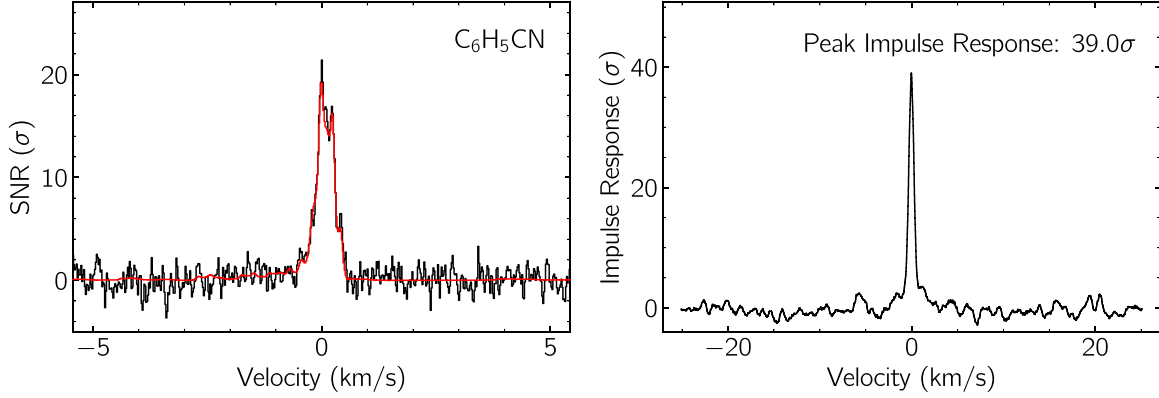


**Figure A3.** Left: velocity-stacked spectra of  $c\text{-C}_6\text{H}_5\text{CN}$  in black, with the corresponding stack of the simulation using the best-fit parameters to the individual lines in red. The data have been uniformly sampled to a resolution of  $0.02 \text{ km s}^{-1}$ . The intensity scale is the signal-to-noise ratio of the spectrum at any given velocity. Right: impulse response function of the stacked spectrum using the simulated line profile as a matched filter. The intensity scale is the signal-to-noise ratio of the response function when centered at a given velocity. The peak of the impulse response function provides a minimum significance for the detection of  $39.0\sigma$ .

**Table A2**

Best-fit Spectroscopic Constants of Ground State Propargyl Cyanide

Constant	Demaison et al. (1985) <sup>a</sup>	This work <sup>b,c</sup>
$A$ (MHz)	19820.1789(22)	19820.080(70)
$B$ (MHz)	2909.59089(33)	2909.6062(12)
$C$ (MHz)	2573.22455(35)	2573.2123(12)
$\Delta_J$ (kHz)	1.86972(15)	1.9046(14)
$\Delta_{JK}$ (kHz)	-67.6822(17)	-67.911(22)
$\Delta_K$ (kHz)	832.439(29)	0.722(69)
$\delta_J$ (kHz)	0.521828(56)	0.52354(82)
$\delta_K$ (kHz)	...	6.35(58)
$\chi_{aa}$ (N) (MHz)	-2.2558(22) <sup>b</sup>	-2.2699(14)

**Table A2**

(Continued)

Constant	Demaison et al. (1985) <sup>a</sup>	This work <sup>b,c</sup>
$\chi_{bb}$ (N) (MHz)	0.2102(29)	0.2154(15)
Number of hfs components	28	112
$\sigma$ (MHz)	0.0017	0.0025
Weighted average	0.847	1.233

**Notes.**<sup>a</sup> Uncertainties ( $1\sigma$ ) are in units of the last significant digit.<sup>b</sup> Hyperfine parameters are from Jager et al. (1990).<sup>c</sup> Derived from the measurements in Table A1.

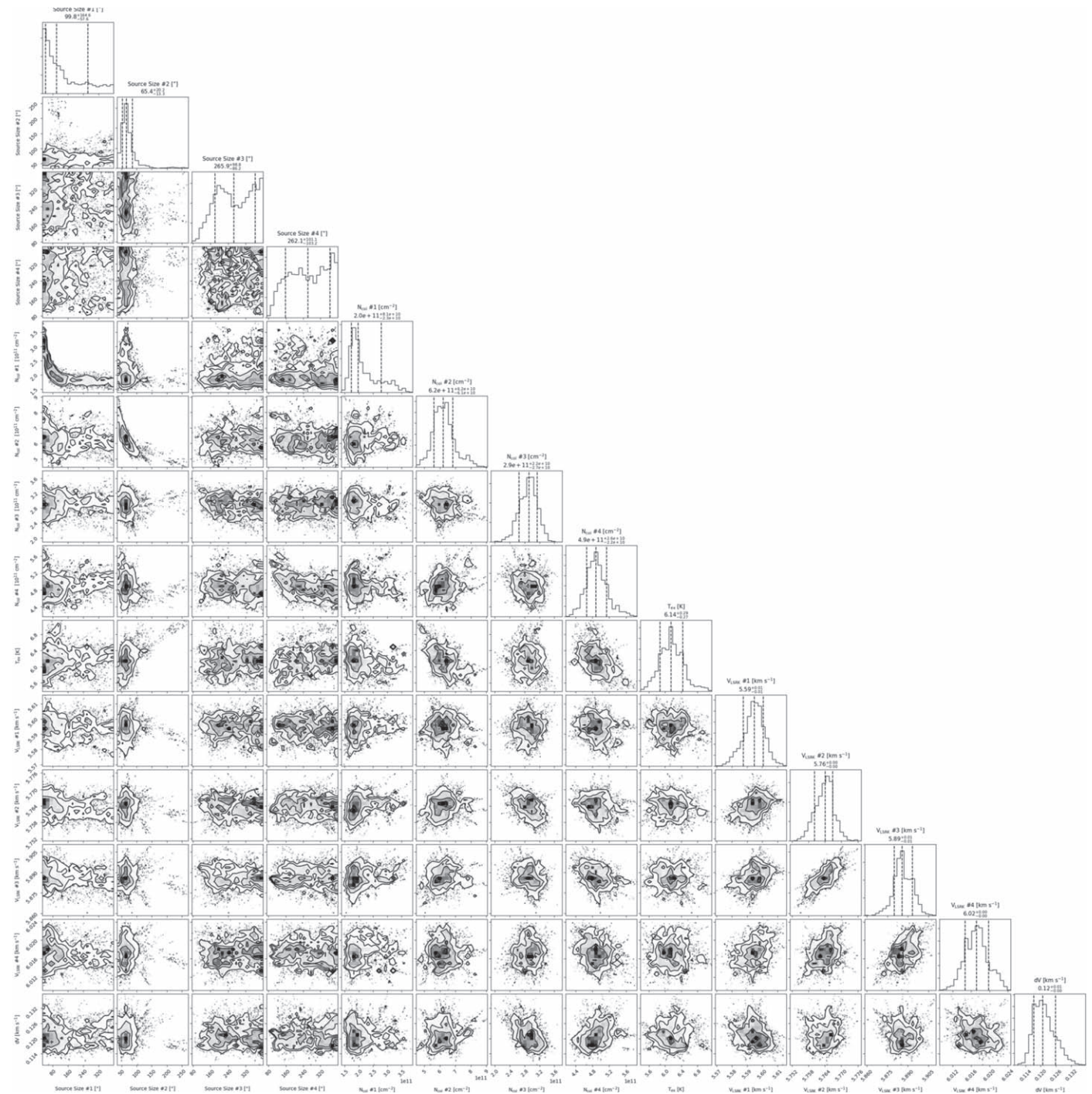


**Figure A4.** Parameter covariances and marginalized posterior distributions for the  $c\text{-C}_6\text{H}_5\text{CN}$  MCMC fit; 16th, 50th, and 84th confidence intervals (corresponding to  $\pm 1\sigma$  for a Gaussian posterior distribution) are shown as vertical lines.



**Table A3**  
Benzonitrile Best-fit Parameters from MCMC Analysis

Component	$v_{\text{lsr}}$ (km s <sup>-1</sup> )	Size ( $''$ )	$N_T^a$ ( $10^{11}$ cm <sup>-2</sup> )	$T_{\text{ex}}$ (K)	$\Delta V$ (km s <sup>-1</sup> )
C1	5.595 <sup>+0.006</sup> <sub>-0.007</sub>	99 <sup>+164</sup> <sub>-57</sub>	1.98 <sup>+0.81</sup> <sub>-0.23</sub>	6.1 <sup>+0.3</sup> <sub>-0.3</sub>	0.121 <sup>+0.005</sup> <sub>-0.004</sub>
C2	5.764 <sup>+0.003</sup> <sub>-0.004</sub>	65 <sup>+20</sup> <sub>-13</sub>	6.22 <sup>+0.62</sup> <sub>-0.61</sub>		
C3	5.886 <sup>+0.007</sup> <sub>-0.006</sub>	265 <sup>+98</sup> <sub>-36</sub>	2.92 <sup>+0.22</sup> <sub>-0.27</sub>		
C4	6.017 <sup>+0.003</sup> <sub>-0.002</sub>	262 <sup>+101</sup> <sub>-103</sub>	4.88 <sup>+0.26</sup> <sub>-0.22</sub>		
$N_T$ (Total) <sup>b</sup>			1.60 <sup>+0.11</sup> <sub>-0.07</sub> × 10 <sup>12</sup> cm <sup>-2</sup>		

**Notes.** The quoted uncertainties represent the 16th and 84th percentile ( $1\sigma$ ) for a Gaussian distribution) uncertainties.

<sup>a</sup> Column density values are highly covariant with the derived source sizes. The marginalized uncertainties on the column densities are therefore dominated by the largely unconstrained nature of the source sizes, and not by the signal-to-noise of the observations. See Figure A4 for a covariance plot, and Loomis et al. (2020) for a detailed explanation of the methods used to constrain these quantities and derive the uncertainties.













<sup>b</sup> Uncertainties derived by adding the uncertainties of the individual components in quadrature.

## Appendix B

### MCMC Fitting Overview

A total of 68 transitions (including hyperfine components) of propargyl cyanide were covered by GOTHAM observations at the time of analysis and were above our predicted flux threshold of 5%, as discussed in Loomis et al. (2020). Of these transitions, none was coincident with interfering transitions of other species, and thus a total of 68 transitions were therefore considered. A total of 156 transitions (including hyperfine components) of benzonitrile were covered by GOTHAM observations at the time of analysis and were above our predicted flux threshold of 5%, as discussed in Loomis et al. (2020). Of these transitions, none was coincident with interfering transitions of other species, and thus a total of 156 transitions were therefore considered. For both species, observational data windowed around these transitions, spectroscopic properties of each transition, and the partition function used in the MCMC analysis are provided in the Harvard Dataverse repository (GOTHAM Collaboration 2020).

### ORCID iDs

Brett A. McGuire  <https://orcid.org/0000-0003-1254-4817>  
 Andrew M. Burkhardt  <https://orcid.org/0000-0003-0799-0927>  
 Ryan A. Loomis  <https://orcid.org/0000-0002-8932-1219>  
 Christopher N. Shingledecker  <https://orcid.org/0000-0002-5171-7568>  
 Kin Long Kelvin Lee  <https://orcid.org/0000-0002-1903-9242>  
 Martin A. Cordiner  <https://orcid.org/0000-0001-8233-2436>  
 Eric Herbst  <https://orcid.org/0000-0002-4649-2536>  
 Emmanuel Momjian  <https://orcid.org/0000-0003-3168-5922>  
 Eric R. Willis  <https://orcid.org/0000-0002-7475-3908>  
 Ci Xue  <https://orcid.org/0000-0003-2760-2119>  
 Anthony J. Remijan  <https://orcid.org/0000-0001-9479-9287>  
 Michael C. McCarthy  <https://orcid.org/0000-0002-5450-5894>

## References

- Agúndez, M., & Wakelam, V. 2013, *ChRv*, **113**, 8710  
 Balucani, N., Asvany, O., Chang, A. H. H., et al. 1999, *JChPh*, **111**, 7457  
 Bell, M. B., Feldman, P. A., Travers, M. J., et al. 1997, *ApJL*, **483**, L61  
 Bradforth, S. E., Kim, E. H., Arnold, D. W., & Neumark, D. M. 1993, *JChPh*, **98**, 800  
 Burkhardt, A. M., Herbst, E., Kalenskii, S. V., et al. 2018, *MNRAS*, **474**, 5068  
 Burkhardt, A. M., Loomis, R. A., Shingledecker, C. N., et al. 2020, *NatAs*, submitted  
 Cernicharo, J., Heras, A. M., Tielens, A. G. G. M., et al. 2001, *ApJL*, **546**, L123  
 Cernicharo, J., Lefloch, B., Agúndez, M., et al. 2018, *ApJL*, **853**, L22  
 Cooke, I. R., Gupta, D., Messinger, J. P., & Sims, I. R. 2020, *ApJL*, **891**, L41  
 Cordiner, M. A., Charnley, S. B., Kisiel, Z., McGuire, B. A., & Kuan, Y.-J. 2017, *ApJ*, **850**, 187  
 Demaison, J., Pohl, I., & Rudolph, H. D. 1985, *JMoSp*, **114**, 210  
 Dobashi, K., Shimoikura, T., Nakamura, F., et al. 2018, *ApJ*, **864**, 82  
 Dobashi, K., Shimoikura, T., Ochiai, T., et al. 2019, *ApJ*, **879**, 0  
 Fehér, O., Tóth, L. V., Ward-Thompson, D., et al. 2016, *A&A*, **590**, A75  
 Fuente, A., Navarro, D. G., Caselli, P., et al. 2019, *A&A*, **624**, A105  
 García-Hernández, D. A., García-Lario, P., Cernicharo, J., Engels, D., & Perea-Calderón, J. V. 2016, *JPhCS*, **728**, 052003  
 Gorshkov, A. G., Ipatov, A. V., Ipatova, I. A., et al. 2016, *AsTL*, **42**, 506  
 GOTHAM Collaboration 2020, Spectral Stacking Data for Phase 1 Science Release of GOTHAM, 1.1, Harvard Dataverse, doi:10.7910/DVN/PG7BHO  
 Gratier, P., Majumdar, L., Ohishi, M., et al. 2016, *ApJS*, **225**, 1  
 Guo, Y., Gu, X., Zhang, F., et al. 2006, *PCCP*, **8**, 5454  
 Hincelin, U., Wakelam, V., Hersant, F., et al. 2011, *A&A*, **530**, A61  
 Jager, W., Krause, H., Mäder, H., & Gerry, M. 1990, *JMoSp*, **143**, 50  
 Jones, B. M., Zhang, F., Kaiser, R. I., et al. 2011, *PNAS*, **108**, 452  
 Jones, H., & Sheridan, J. 1982, *JMoSt*, **78**, 303  
 Kaifu, N., Ohishi, M., Kawaguchi, K., et al. 2004, *PASJ*, **56**, 69  
 Kraemer, K. E., Sloan, G. C., Bernard-Salas, J., et al. 2006, *ApJL*, **652**, L25  
 Lee, K. L. K., McGuire, B. A., & McCarthy, M. C. 2019, *PCCP*, **21**, 2946  
 Lias, S. G., Levin, R. D., & Kafali, S. A. 2020, NIST Chemistry WebBook, NIST Standard Reference Database No. 69 (Gaithersburg, MD: National Institute of Standards and Technology)  
 Lipkus, A. H., Yuan, Q., Lucas, K. A., et al. 2008, *The Journal of Organic Chemistry*, **73**, 4443  
 Loomis, R. A., Burkhardt, A. M., Shingledecker, C. N., et al. 2020, *NatAs*, submitted  
 Loomis, R. A., Shingledecker, C. N., Langston, G., et al. 2016, *MNRAS*, **463**, 4175  
 Lovas, F. J., Remijan, A. J., Hollis, J. M., Jewell, P. R., & Snyder, L. E. 2006, *ApJL*, **637**, L37  
 Malek, S. E., Cami, J., & Bernard-Salas, J. 2012, *ApJ*, **744**, 16  
 McCarthy, M. C., Lee, K. L. K., Loomis, R. A., et al. 2020, *NatAs*, submitted  
 McGuire, B. A. 2018, *ApJS*, **239**, 17  
 McGuire, B. A., Burkhardt, A. M., Kalenskii, S. V., et al. 2018, *Sci*, **359**, 202  
 McGuire, B. A., Loomis, R. A., Burkhardt, A. M., et al. 2020, *Sci*, submitted  
 McNaughton, D., Romeril, N. G., Lappert, M. F., & Kroto, H. W. 1988, *JMoSp*, **132**, 407  
 Morgan, M., White, S., Lockman, J., et al. 2008, in Union Radio Scientifique Internationale XXIX General Assembly, J02p1  
 Onishi, T., Mizuno, A., Kawamura, A., Tachihara, K., & Fukui, Y. 2002, *ApJ*, **575**, 950  
 Perley, R. A., & Butler, B. J. 2017, *ApJS*, **230**, 0  
 Rosh, D. A., Bloss, M., Brandt, P., et al. 2012, *IEEE*, 12354148, 1  
 Ruaud, M., Wakelam, V., & Hersant, F. 2016, *MNRAS*, **459**, 3756  
 Ruddigkeit, L., van Deursen, R., Blum, L. C., & Reymond, J.-L. 2012, *Journal of Chemical Information and Modeling*, **52**, 2864  
 Scibelli, S., & Shirley, Y. 2020, *ApJ*, **891**, 73  
 Selina, R. J., Murphy, E. J., McKinnon, M., et al. 2018, in ASP Conf. Ser. 517, Science with a Next Generation Very Large Array, ed. E. Murphy (San Francisco, CA: ASP), 15  
 Smith, I. W. M., Sage, A. M., Donahue, N. M., Herbst, E., & Quan, D. 2006, *FaDi*, **133**, 137  
 Tielens, A. G. G. M. 2008, *ARA&A*, **46**, 289  
 Turner, B. E. 1991, *ApJS*, **76**, 617  
 Ulich, B. L., & Haas, R. W. 1976, *ApJ*, **30**, 247  
 Wakelam, V., Loison, J.-C., Herbst, E., et al. 2015, *ApJS*, **217**, 20  
 Watson, J. K. G. 1977, in *Vibrational Spectra and Structure*, ed. J. R. Durig (New York: Merceel Dekker), 1  
 Woon, D. E., & Herbst, E. 2009, *ApJS*, **185**, 273  
 Xue, C., Willis, E. R., Loomis, R. A., et al. 2020, *ApJL*, **900**, L9